

Numerical Evaluation of the $e^+e^- \rightarrow \mu^+\mu^-$ Cross Section in the Standard Model

Alex Pearce

April 11, 2012

Abstract

The Standard Model's (SM) prediction of particles beyond those initially considered by quantum electrodynamics (QED) has yielded excellent results. The Super Proton Synchrotron (SPS) at CERN recently detected both the W bosons and the Z boson via the $p\bar{p}$ channel (Rubbia, van der Meer et al.). We performed a numerical integration of the differential cross section of the $e^+e^- \rightarrow \mu^+\mu^-$ scattering process with a trapezium and a Monte Carlo algorithm in the hope that the proposed Large Electron-Positron collider (LEP) will verify this channel of Z production. A large resonance at $\sqrt{s} = 91.21 \pm 0.01$ GeV was found, slightly above the Z mass. The peak cross section was found to be $\sigma = (5.13 \pm 0.19) \times 10^{-6} \text{ GeV}^{-2} = 2.00 \pm 0.07 \text{ nb}^{-1}$. Implementing the algorithms in C was found to be nearly 50 times faster than in Python.

1 Introduction

The proposition of three mediators of the weak nuclear force, the W^+ , W^- and Z bosons, has been all but proven by the current SPS team at CERN. The suggestion of Z production via electron-positron pairs is now becoming of interest to experimentalists. The process manifests itself by an electron-positron pair (e^-e^+) annihilating, forming either a virtual photon or Z boson, and then a muon-antimuon pair ($\mu^-\mu^+$) being produced.

This interaction is described by the Feynman diagram in figure 1a. The scattering is also described by a t-channel diagram (in figure 1b), however we proceed by analysing the s-channel, as it is only via this channel which we may measure resonances and new unstable particles. Note that a u-channel diagram also exists, but it is merely a swapping of the outgoing particles' momenta in the t-channel. We ignore the u-channel for this reason.

Feynman diagrams allow us to apply the Feynman rules thus to producing a matrix element \mathcal{M} . The square of the matrix element corresponds to a differential cross section $\frac{d\sigma}{d\Omega}$ which may be integrated to find the total cross section σ , which is measurable by a detector.

The following section briefly outlines the theory behind the interactions. The integration methods used to evaluate the differential cross sections are explored

in the section 3, along with a study of the differential cross sections in order to judge the effectiveness of numerical integration upon them. The results are presented and analysed in section 4, then a discussion of the kinematic variables follows in section 5. A brief discussion on performance is given in section 6, and finally some concise conclusions are drawn in section 7.

2 Principles of Interaction Cross Sections

With reference to the Feynman diagrams in figures 1a and 1b, the incoming particles are labelled with the four-momenta p_1^ν and p_2^ν , whilst the outgoing particles carry p_3^ν and p_4^ν . At LEP, the electrons and positrons will be accelerated around a loop in opposite directions. The collider energy is then given by \sqrt{s} , where

$$s = (p_1 + p_2)^2.$$

Here we have suppressed the metric tensor and the covariant notation, implicitly assuming four vectors. The collider energy is then analogous to the hypotenuse of a right-angled triangle of sides p_1^ν and p_2^ν .

The differential cross sections are dependant on the collider energy via the dimensionless variables

$$\varepsilon = \frac{m_\mu}{\sqrt{s}}, \quad \lambda = \frac{M_Z}{\sqrt{s}},$$

where m_μ is the muon mass. It is worth noting the energies LEP will be operating at allow us to take the electron as massless in the ultrarelativistic limit.¹

2.1 Real and Virtual Particles

As noted in figure 1a, the scattering may be mediated by either a virtual photon γ^* or a $Z^{(*)}$ boson, where the bracketed star notation indicates that the boson may be either *on-* or *off-mass-shell*. These terms refer to how well the mediating particles (propagators in the Feynman diagrams) adhere to the mass-energy relation $E^2 - |\vec{p}|^2 c^2 = m^2 c^4$. Propagators exceeding the classical relativistic values of E and p are off-shell, and said to be virtual particles. This violation of relativity is allowed because it is permitted by the Heisenberg uncertainty principle $\Delta E \Delta t \geq \hbar$; the violation in energy may only exist for a very short period of time.

The Z boson will be on-shell (i.e. real) if and only if $s = M_Z^2$, where M_Z is the boson's mass. When the particle is real, we can detect it. With this, we should expect a cross section resonance as the boson tends towards being on-shell.

¹In addition the muon is over 200 times more massive than the electron so we may disregard the electron mass in scattering interactions.

2.2 Differential Cross Sections

The total matrix element \mathcal{M} must be considered as it is the integrated square of this that LEP will detect. As the propagator in the interaction may be one of two particles, \mathcal{M} must be the sum of two separate matrix elements (one matrix element for each possible propagator). The measurable quantity, the cross section σ , is the integrated square of the matrix element, so we must have the square of a sum:

$$\begin{aligned}\mathcal{M} &= \mathcal{M}_\gamma + \mathcal{M}_Z, \\ \mathcal{M}^2 &= (\mathcal{M}_\gamma + \mathcal{M}_Z)^2 \\ &= \mathcal{M}_\gamma^2 + \mathcal{M}_Z^2 + 2 \operatorname{Re}(\mathcal{M}_\gamma \mathcal{M}_Z^*) \\ &= \frac{d\sigma^{\gamma-\gamma}}{d\Omega} + \frac{d\sigma^{Z-Z}}{d\Omega} + \frac{d\sigma^{\gamma-Z}}{d\Omega} \\ &= \frac{d\sigma}{d\Omega}.\end{aligned}$$

Each term of \mathcal{M}^2 corresponds to its own differential cross section: the first for the pure photon process, the second for the pure Z process, and the last for the interference of both processes.

The functional form of each differential cross section is derived by applying the Feynman rules to figure 1a. They are given in appendix A.

Plots of the differentials are given in section 8.2. Figures 2, 3, and 4 show a pair of plots for increasing collider energies $\sqrt{s} = 3 \text{ GeV}$, M_Z , and 115 GeV respectively. The left-hand figure in each pair shows just the QED differential while the right-hand side figure shows the full Standard Model differential.

The full Standard Model distribution only slightly alters the QED distribution in the low energy regime, namely by introducing a small asymmetry in the quadratic form of the curve. The Standard Model contribution is much more prominent for the M_Z regime as, not only does it introduce an asymmetry, it shifts the position of the curve along $\frac{d\sigma}{d\Omega}$ by two orders of magnitude. This should result in a large cross section σ around this region.

The Standard Model differential has a very different form in the high energy regime whilst also increasing the magnitude of the curve. These plots show that the Standard Model contribution tends to increase the cross section of the scattering. In particular, we expect to see a large peak in σ around M_Z .

3 Integration of the Differential $\frac{d\sigma}{d\Omega}$

A common approach to numerically approximating integrals is the trapezium rule. We shall use the trapezium rule and compare it with the more recent Monte Carlo method, whereby random points are sampled and the fraction of those between the curve and the independent axis is proportional to the area i.e. the integral.

The reasoning behind using two methods of numerical integration is twofold. Firstly, it serves as a consistency check: if at least one method is running incorrectly, the results from each are unlikely to agree with each other. Secondly, the data collected with respect to the efficiency of each method on the given functions may be useful for future analysis of particle interaction cross sections. (Indeed, the collected data may be useful for analysing any functions of a similar form.)

On this point, it is worth noting that the accuracy of each algorithm will depend largely on the functional form of the differential cross sections. Erratic, non-analytic functions will be poorly suited for trapezium evaluation, while functions with very small variations will result in inaccurate Monte Carlo evaluation. The differential forms are plotted in figures 2, 3 and 4. The impact of these forms in the accuracy of the final results will be analysed in section 4.

3.1 Method

Firstly, we observe that there is no ϕ dependence in any of the differential cross sections. This makes the integration over ϕ trivial ($0 \leq \phi \leq 2\pi$), adding a factor of 2π to cross section σ . This simplifies the problem significantly as we are now dealing with a one-dimensional integral and so may use the trapezium rule.

As the integration is over circular polar coordinates, we note that the differential $\sin \theta \, d\theta \, d\phi$ may be expressed as $d(\cos \theta) \, d\phi$, hence we may perform the change of variable $\cos \theta \rightarrow x$. This changes the limits in θ to the limits in x

$$0 \leq \theta \leq \pi \rightarrow -1 \leq x \leq 1.$$

Consequently, the random numbers generated for the Monte Carlo integration are generated between -1 and 1, providing a uniform distribution in $\cos \theta$, rather than θ .

A simple Monte Carlo integration will be performed via

$$\int_a^b f(x) \, dx \approx \frac{b-a}{N} \sum_{i=1}^N f(x_i),$$

where N is the number of random points to be sampled and x_i is the i^{th} random number within the limits of integration.

A similarly simple trapezium algorithm is used:

$$\int_a^b f(x) \, dx \approx \frac{h(f(a) + f(b))}{2} + h \sum_{i=1}^{N-1} f(a + ih), \quad h = \frac{b-a}{N}.$$

h is the trapezium width and N is the number of trapezia used to estimate the integral with.

Both methods are quoted as approximations, but it should be considered that as $N \rightarrow \infty$ the Monte Carlo method becomes exact, despite this being impossible to perform computationally.

The number of points to sample or the number of trapezia to use will depend on the computational power and time available, as well as the accuracy and precision desired. The exact values used will be discussed in the following section.

We note that the problem may be tackled in two distinct ways. We may either sum the integrands and integrate the resulting function, or we can integrate the differentials and then sum the results. We will comment further on this point in section 4.2.

4 Results and Analysis

When numerically integrating the differential cross sections, they were evaluated in collider energy steps of 0.01 GeV so as to allow fine detail in the plots and precise readings. 1000 trapezia were used in the trapezium algorithm, while 1000 random points were sampled with the Monte Carlo method. Although it is not the case that N trapezia should produce similarly accurate or precise values as N sampled points, it was found that $N = 1000$ for both algorithms allowed for both a fast enumeration of the integrals and consistent results with each other.

The integrated cross section is presented in figures 6a and 6b. Each plot shows both the trapezium and Monte Carlo integration results, but their correspondence is such that they are almost indistinguishable from one another.

The Monte Carlo cross section shows slight fluctuations on a scale of 10^{-8} GeV^{-2} but its form follows that of the trapezium evaluation precisely.

4.1 Resonance

There is a striking resonance around the Z mass M_Z . The cross section peaks to $5.13 \times 10^{-6} \text{ GeV}^{-2}$ at collider energy 91.21 GeV. It is important to note that this is *above* the Z mass of 91.19 GeV. The explanation for this cannot be found in the $\gamma - \gamma$ channel as there is clearly no resonance in its cross section (figure 6a). It is due to the Standard Model contribution, and in particular the interference term $\gamma - Z$.

Figure 8b shows the cross section for the interference term as evaluated by the Monte Carlo method, with the trapezium algorithm superimposed. Figure 8a shows just the trapezium algorithm's evaluation. We see from the trapezium-evaluated cross section that the contribution at $\sqrt{s} = M_Z$ is 0, but past the Z boson mass the contribution is positive. Thus, the interference terms shifts the resonance to slightly higher energies.

The resonance itself is due to the $Z - Z$ term. We see an increase in the cross section in an energy range around M_Z because it is in this range that the Z boson becomes on-shell, and hence becomes real and detectable. The resonance is our detection of the Z boson mediating the scattering interaction.

Recalling the previously mentioned Heisenberg uncertainty principle, ΔE is the width of the resonance at half maximum and then $\Delta t = \frac{\hbar}{\Delta E}$ corresponds

to the lifetime of the Z boson. A rough reading off of figure 9 gives $\Delta E = 2.5 \pm 0.25$ GeV and therefore $\Delta t = \tau = (2.6 \pm 0.3) \times 10^{-25}$ s. It is now clear that the parameter Γ_Z is the resonance width at half maximum.

Note that, from figure 8a, the interference term γ - Z contributes nothing at M_Z .

4.2 Interference Term γ - Z

TODO: why does the interference term has the form it does.

The Monte Carlo integration of $\frac{d\sigma}{d\Omega}^{\gamma-Z}$ shown in figure 8b reveals a spectacular failing of the algorithm. Despite its satisfactory performance evaluating all other cross sections, the algorithm fails on integrating the form of the cross section, shown in figure 5.

We believe that this failing is due to the near-linear form of the integrand. Inspection may conclude that the function is linear, but viewed over a wider range in $\cos\theta$ the function is non-linear, resembling a quadratic form. The range $-1 \leq \cos\theta \leq 1$ is zoomed in on a small segment of a curved line so closely approximates a linear function. The Monte Carlo approach has great difficulty in accurately evaluating the integral in this case as many sampled points, more than could be available given reasonable time constraints, are required to account for the incredibly subtle functional form. This subtly results in very erratic behaviour on numerical evaluation, resulting in both inaccurate and inconsistent results. The trapezium rule allows for this subtly, producing consistent results.

Figure 8 also shows that the Monte Carlo method's erratic behaviour produces a γ - Z cross section an order of magnitude larger the trapezium result. Due to this, the Monte Carlo resonance peak varies, by $\pm 0.5 \times 10^{-7}$ GeV $^{-2}$. Its position and value fluctuates around the trapezium peak on subsequent trials. The performance differences of each method is discussed in section 6.

As touched on in section 3.1, we may sum the integrands and integrate the resulting function. If we take this approach, the subtleties of the interference term are absorbed into the other differentials. Integrating the sum therefore eliminates the only major problem in using the Monte Carlo algorithm.

Due to this, we use the final peak cross section from the trapezium evaluation and use the Monte Carlo evaluation to determine the errors. We recorded a peak resonance of $\sigma = (5.13 \pm 0.19) \times 10^{-6}$ GeV $^{-2} = 2.00 \pm 0.07$ nb $^{-1}$ at a collider energy of $\sqrt{s} = 91.21 \pm 0.01$ GeV.

5 Kinematic Variables

TODO: Discussion of $\cos\theta$ and $p_T = |\vec{p}_f| \sin\theta$.

6 Performance

Although the trapezium and Monte Carlo methods of numerical integration produced similarly accurate results in negligibly different times, it should be possible to evaluate the integrals quicker.

The reasoning behind this claim is that we have used Python, a scripting language, to solve the problem. Python is generally slower than a compiled language such as FORTRAN or C.

In order to measure any benefits that a compiled language might bring, the Python script was timed over several runs of numerically integrating then summing the separate differential cross sections. This time was averaged to give an approximate runtime estimate.

The parameters used were a collider energy running from 3 GeV to 200 GeV in steps of 0.1 GeV. The number of trapezia used was 1000.

After 50 runs of the Python script, the average runtime was 18.7 ± 0.2 s.

A C script was then written which performed the same numerical integrations as the Python script, and again was ran 50 times to find an average runtime. It was found that the C script took an average of 0.40 ± 0.1 s. A plot of the data produced by the C script is given in ???. It shows that each script produces equal results.

This shows a large difference in performance between the two languages. The C script ran in $2.1 \pm 0.1\%$ of the time the Python script required.

The program is extremely repetitive; the parameters given above require close to 2 million iterations of the integration algorithm. The C compiler's ability to make optimisations in the script save small amounts of time per iteration, which are compounded to produce vast improvements in the total runtime.

Using the Python script, summing the individual integrals takes an almost-equal execution time as summing the integrands and then integrating. Interestingly, the C script takes 0.03 ± 0.01 s less to sum the integrands.

7 Conclusions

A numerical integration of the $e^+e^- \rightarrow \mu^+\mu^-$ scattering cross section was performed in order to analyse its behaviour over a range of collider energies. A resonant behaviour was found near the Z boson mass. Both algorithms performed well, integrating the differentials quickly and accurately, although the Monte Carlo algorithm required substantially more computations to achieve similar precision to the trapezium rule. In order to overcome the subtlety in the interference differential cross section, integrating the sum of the differentials is the better approach for Monte Carlo evaluation. The trapezium rule proved to be the more efficient algorithm in this one dimensional case. In higher order problems, the Monte Carlo approach must be carefully analysed to ensure accurate results. Finally, using C produced drastically faster results than when using Python. Using C also allowed a noticeable speed improvement when integrating the sum of the integrands, rather than summing the integrated differentials.

8 Figures

8.1 Feynman Diagrams

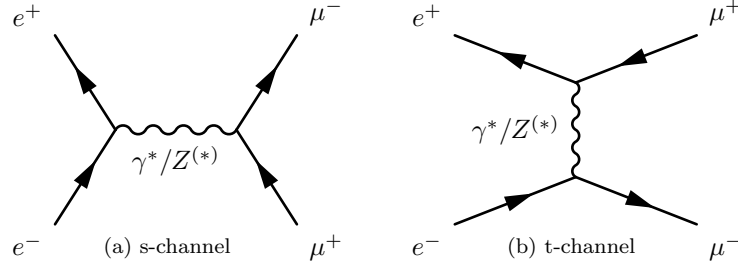


Figure 1: $e^-e^+ \rightarrow \mu^-\mu^+$ scattering via two different channels. Time flows from left to right.

8.2 Differential Cross Sections

This subsection contains plottings of the QED differential cross section (γ - γ channel) and then the full Standard Model cross section (γ - γ , Z - Z and γ - Z channels) at three different collider energies.

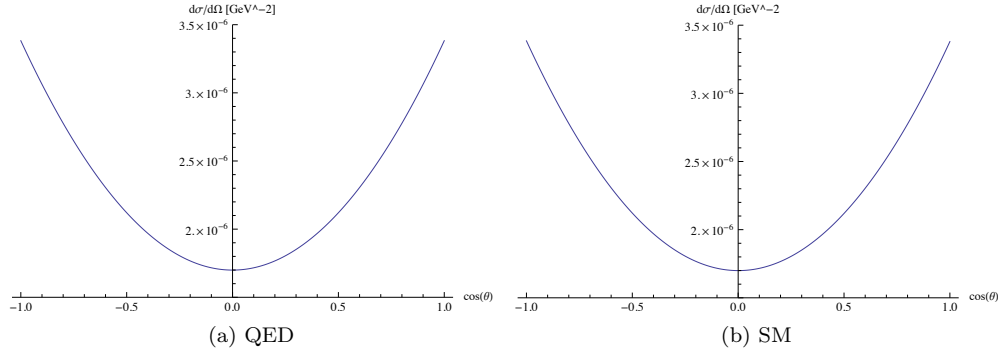


Figure 2: $\frac{d\sigma}{d\Omega}$ at $\sqrt{s} = 3$ GeV.

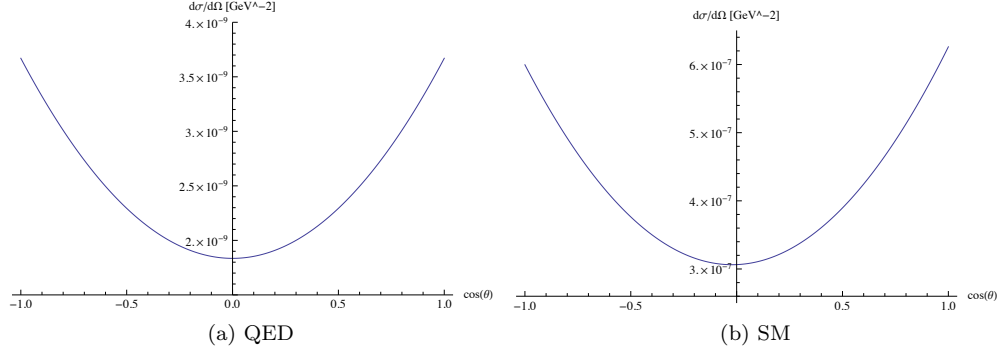


Figure 3: $\frac{d\sigma}{d\Omega}$ at $\sqrt{s} = M_Z = 91.19$ GeV.

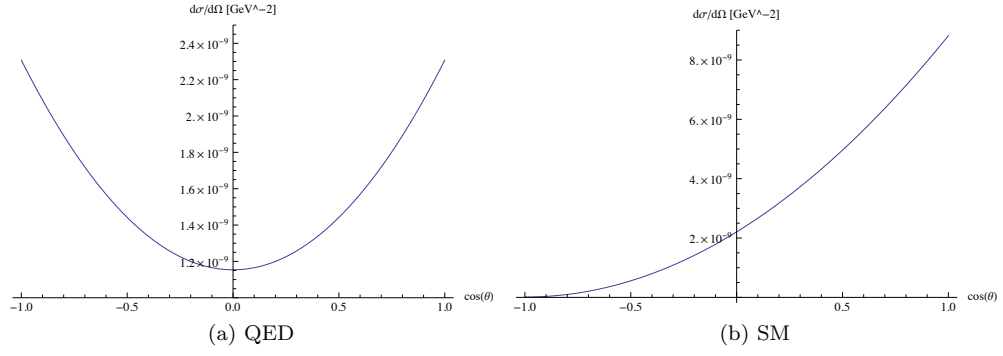


Figure 4: $\frac{d\sigma}{d\Omega}$ at $\sqrt{s} = 115$ GeV.

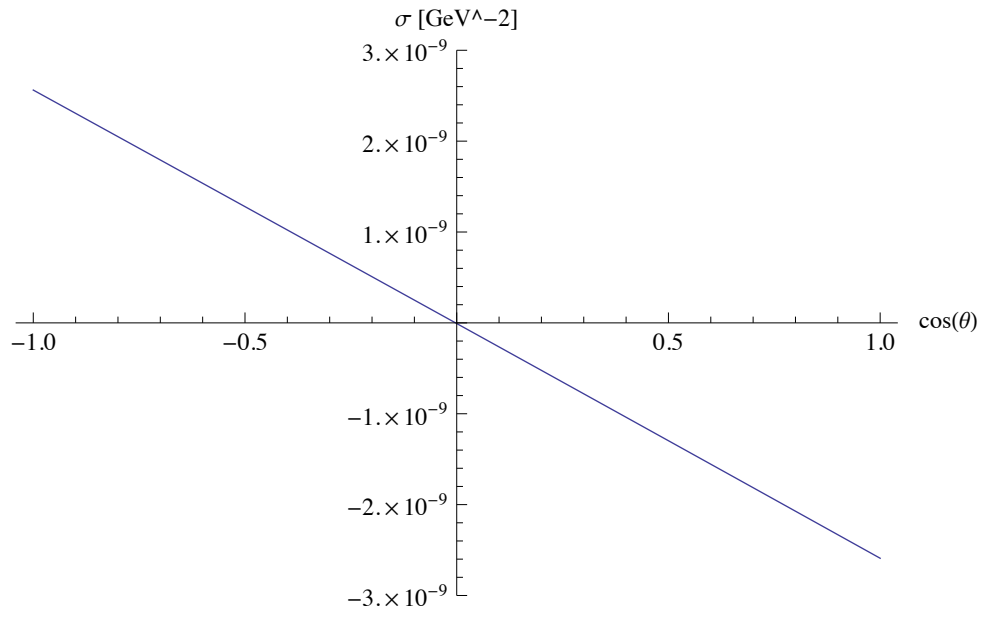


Figure 5: $\frac{d\sigma}{d\Omega}^{\gamma-Z}$ at $\sqrt{s} = 3$ GeV.

8.3 Cross Sections σ

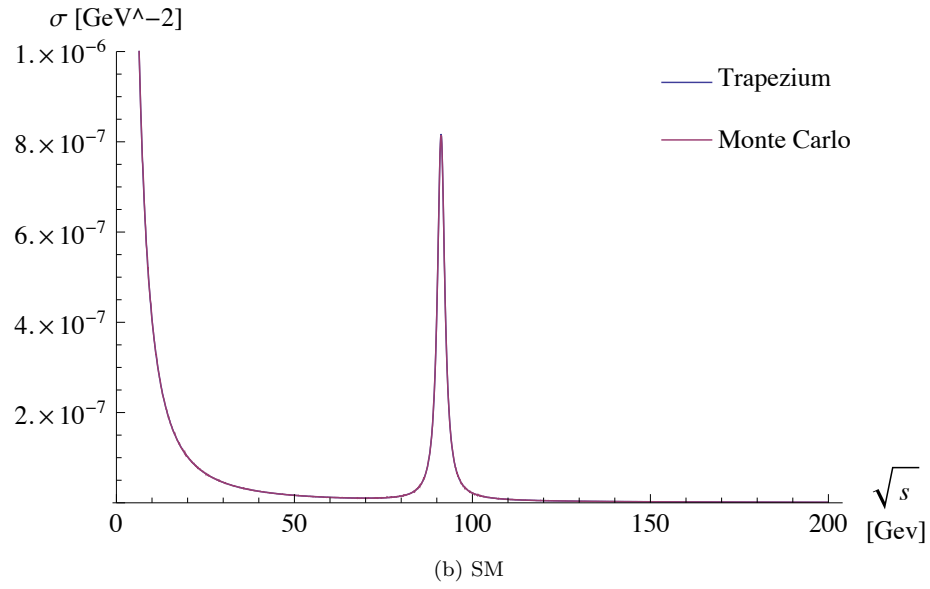
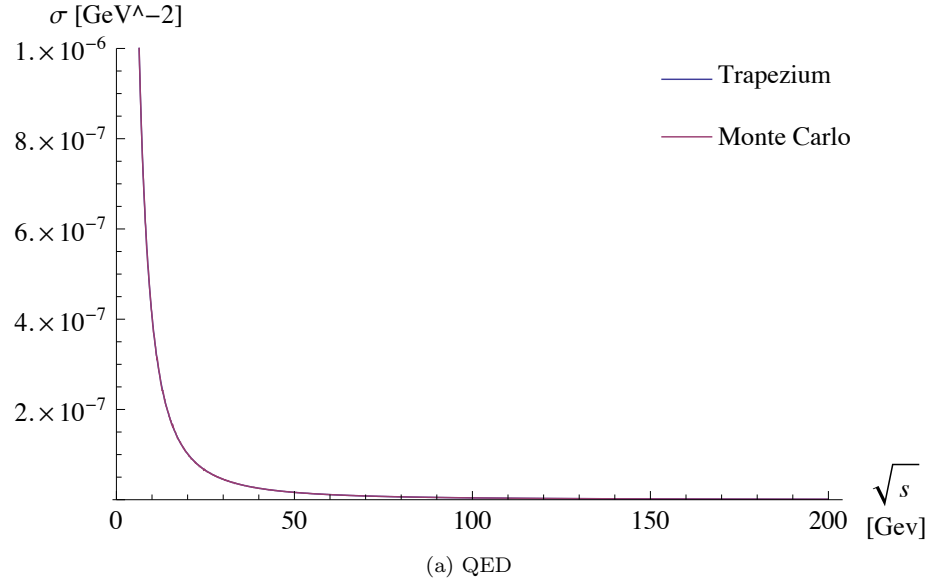


Figure 6: Trapezium and Montecarlo cross section σ for collider energies 3-200 GeV.

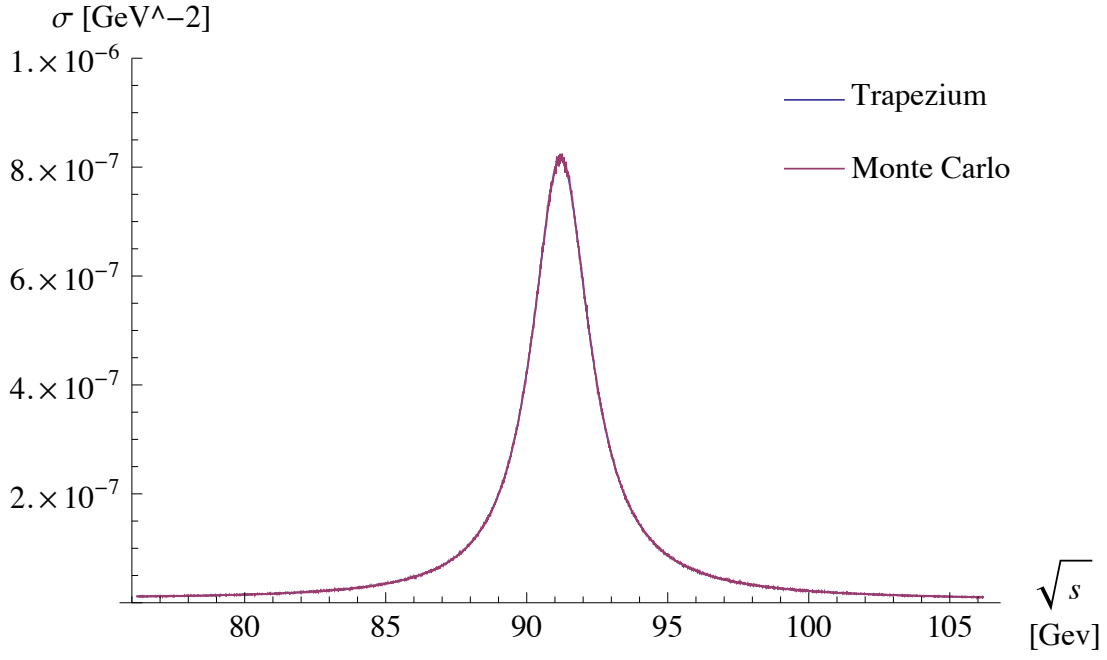


Figure 7: Trapezium and Montecarlo cross section σ for collider energies centred 15 GeV around M_Z .

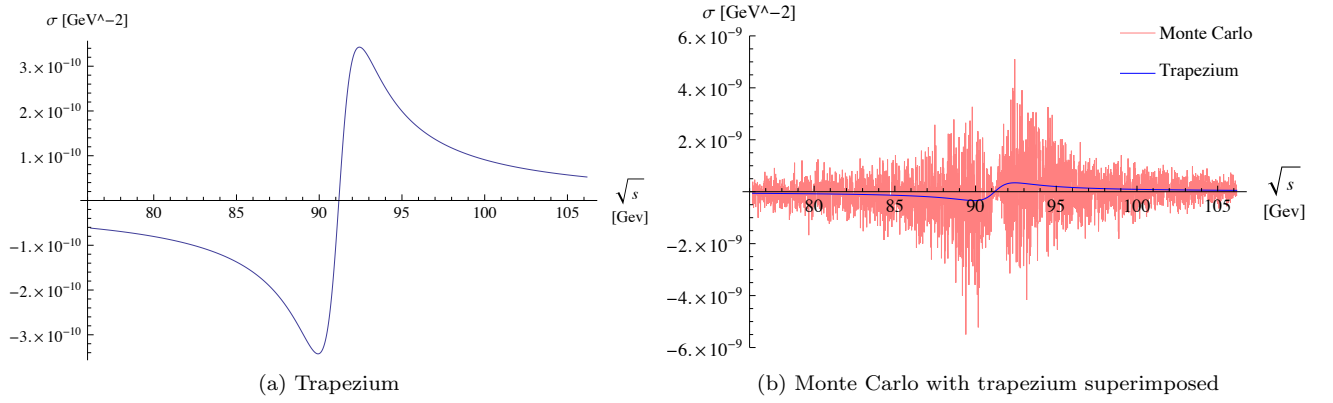


Figure 8: γ - Z cross section for collider energies centred 15 GeV around M_Z .

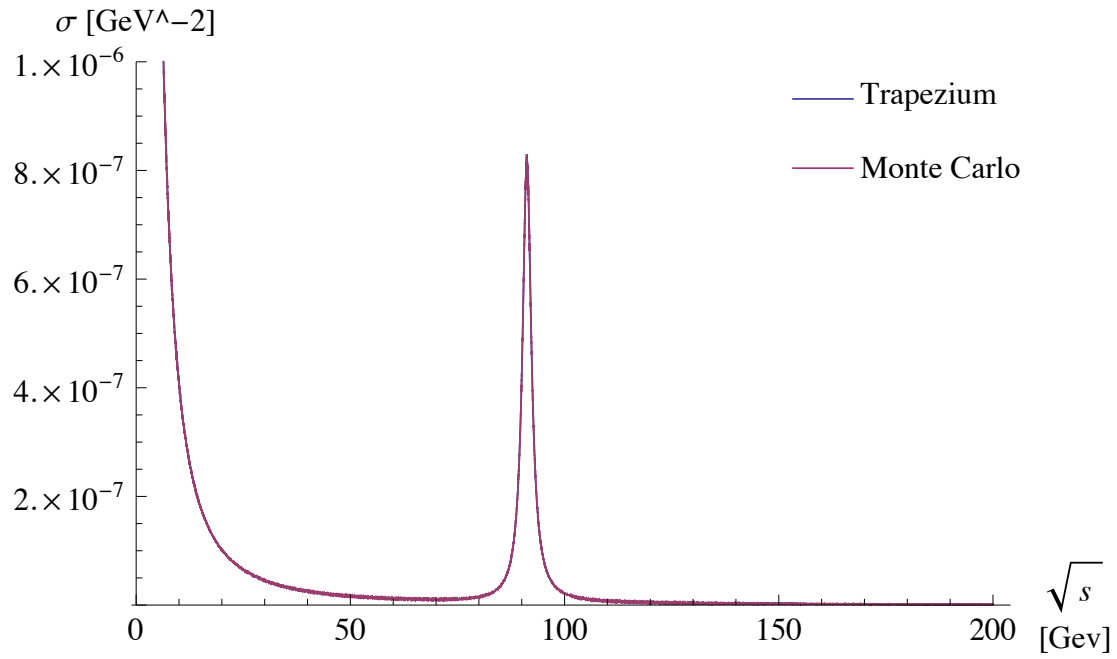


Figure 9: Trapezium and Montecarlo cross section σ for collider energies from 3 GeV to 200 GeV. This data was produced by a C script, whereas all other plots use data from a Python script.

A Differential Cross Sections

The cross sections corresponding to the photon, Z , and interference matrix elements follow. Due to the length of the analytic solutions, constants are defined, then the cross section is defined with respect to these constants.

The small energy scales that will be reachable at LEP allow us to take the couplings g_e and g_z as constant. We define $g_e = \sqrt{4\pi\alpha}$ and $g_z = \sqrt{4\pi\alpha}(\cos\theta_w \sin\theta_w)^{-1}$.²

A.1 $\gamma - \gamma$

Define

$$\alpha = \frac{g_e^4}{(8\pi)^2 s} \sqrt{1 - 4\varepsilon^2}.$$

Then

$$\begin{aligned} \frac{d\sigma^{\gamma-\gamma}}{d\Omega} &= \alpha(1 + \cos^2\vartheta + 4\varepsilon^2 \sin^2\vartheta), \\ \sigma^{\gamma-\gamma} &= \frac{16\pi\alpha}{3}(1 + 2\varepsilon^2). \end{aligned} \tag{1}$$

A.2 $Z - Z$

Define

$$\begin{aligned} \alpha &= \frac{g_Z^4}{(32\pi)^2 s} \frac{\sqrt{1 - 4\varepsilon^2}}{(1 - \lambda^2)^2 + (\frac{\lambda\Gamma_Z}{\sqrt{s}})}, \\ \beta &= ((C_V^e)^2 + (C_A^e)^2)((C_V^\mu)^2), \\ \Gamma &= ((C_V^e)^2 + (C_A^e)^2)((C_A^\mu)^2)(1 - 4\varepsilon^2), \\ \Delta &= 8C_V^e C_A^e C_V^\mu C_A^\mu \sqrt{1 - 4\varepsilon^2}. \end{aligned}$$

Then

$$\begin{aligned} \frac{d\sigma^{Z-Z}}{d\Omega} &= \alpha(\beta(1 + \cos^2\vartheta + 4\varepsilon^2 \sin^2\vartheta) + \Delta(1 + \cos^2\vartheta) + \Gamma \cos\vartheta), \\ \sigma^{\gamma-\gamma} &= \frac{16\pi\alpha}{3}(\Gamma + (1 + 2\varepsilon^2)\beta). \end{aligned} \tag{2}$$

² α is taken to be $\frac{1}{128}$, $\sin^2\theta_w$ is taken to be 0.23152.

A.3 γ - Z

Define

$$\begin{aligned}\alpha &= \frac{g_Z^4}{(32\pi)^2 s} \frac{\sqrt{1-4\varepsilon^2}}{(1-\lambda^2)^2 + (\frac{\lambda\Gamma_Z}{\sqrt{s}})}, \\ \beta &= ((C_V^e)^2 + (C_A^e)^2)((C_V^\mu)^2), \\ \Gamma &= ((C_V^e)^2 + (C_A^e)^2)((C_A^\mu)^2)(1-4\varepsilon^2), \\ \Delta &= 8C_V^e C_A^e C_V^\mu C_A^\mu \sqrt{1-4\varepsilon^2}.\end{aligned}$$

Then

$$\begin{aligned}\frac{d\sigma^{\gamma-Z}}{d\Omega} &= \alpha(\beta(1 + \cos^2 \vartheta + 4\varepsilon^2 \sin^2 \vartheta) + \Delta \cos \vartheta), \\ \sigma^{\gamma-Z} &= \frac{16\pi\alpha\beta}{3}(1 + 2\varepsilon^2).\end{aligned}\tag{3}$$

References